Nuclear Instruments and Methods in Physics Research A 371 (1996) 96–115

ELSEVIER

NUCLEAR INSTRUMENTS & METHODS IN PHYSICS RESEARCH Section A

CsI-photocathode and RICH detector

F. Piuz

CERN, Geneva, Switzerland

Abstract

The development of fast RICH detectors using solid photoconverters is reviewed in the context of basic research and applications to high-energy physics experiments. The novel layout of the CsI fast RICH and the associated technologies are discussed in view of design optimization. Experimental results are presented and discussed in relation to photoelectric yield, detector efficiency and stability, Cherenkov resolutions, background, ageing and pattern recognition.

1. Introduction to a second generation of RICH detector: the CsI fast RICH

The requirements set by the future accelerators on the parameters of high-energy physics (HEP) experiments, such as event rate and multiplicities, have, in the last 4 to 5 years, prompted intense activity in all fields of detector R&D: tracking, particle identification (PID) and calorimetry. In this paper, we shall review some aspects of that effort in the field of PID using the Ring Imaging technique (RICH).

Let us first recall two of the experimental challenges to be met at the LHC: twenty inelastic events every 25 ns in p–p mode or multiplicity up to 8000 charged particles in one pseudorapidity unit every ms in Pb–Pb mode. The only choices left for imaging detectors able to cope with such constraints are those based on the fast RICH layout [1] or on fast detecting elements such as photomultipliers or hybrid photodiodes (HPD) [2]. The fast RICH detector, on which we shall concentrate in this report (Fig. 1) has the features required such as a thin sensitive volume allowing for minimum occupation time (20–30 ns), and the potential of achieving recognition of very dense event patterns due to the 2-dimensional readout of a cathode segmented into pads of ~0.5–1.0 cm^2.

Whatever the radiator choice, gaseous or liquid, the photodetector (MWPC) has to have a photoconversion gap as thin as possible in order to keep to a minimum the parallax error, inherent to the fast RICH layout, in the localization of the photoelectrons. Also, since in the case of a proximity focusing geometry with solid or liquid radiators, the charged particles (MIP) do cross the photodetector: a very thin sensitive volume prevents the heavily ionizing MIP from obscuring the ring patterns, permitting good localization of the particle impacts. For these reasons, the best gaseous photoconverter is the TEA vapour which has, at normal temperature, a photoabsorption mean free path (MFP) of a fraction of a millimeter. That choice implies the use of CaF_2 windows for containment of the MWPC gas (Fig. 1a), restricts the number of suitable radiators (noble gases, LiF, NaF, SiO_2, etc.), i.e. components possibly too expensive for a very large system. On the other hand, the TMAE vapour, the spectral sensitivity of which allows the use of quartz windows, has a comparatively low vapor pressure which imposes the use of a relatively high operation temperature to allow one to keep the photoconversion gap small enough.

These technical considerations have determined the design of a large HEP RICH detector at CERN for the NA45 Experiment, the CERES RICH [3] and, on a smaller scale, subject to severe constraints, the CAPRICE RICH detector [4] used in an astrophysics experiment. Another large RICH system, based on TEA and LiF radiator is under development at CLEO [5].

A decisive step was taken when Seguinot et al. [6] demonstrated that a thin solid film of CsI could be used as

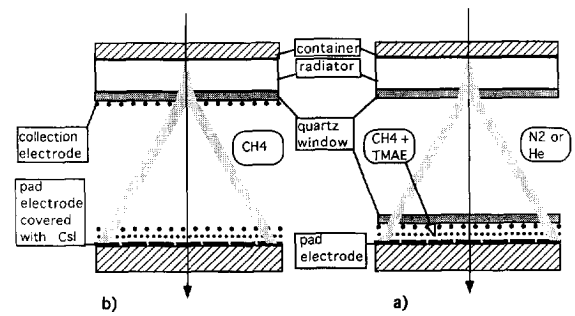

Fig. 1. Schematic view of the fast-RICH layout using a liquid C_6F_{14} radiator operated with (a) TMAE vapour, which is enclosed by a second quartz window, with a UV transparent gas being circulated in the proximity gap and (b) CsI covering the pad cathode where only CH_4 is circulated in the whole gap and a collection grid is added close to the radiator.

SSDI 0168-9002(95)01442-X

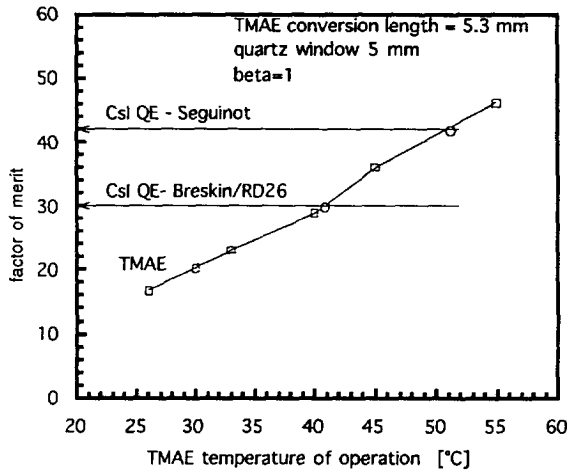

Fig. 2. Comparison of the factors of merit of a fast-RICH operated with CsI and TMAE in a photoconversion gap of 5.3 mm and a 5 mm thick quartz window. Arrows refer to (1) average CsI QE and (2) best CsI QE, shown in Fig. 4. The factor of merit is plotted against the temperature at which a fraction 1/e of the photons are converted in the 5.3 mm gap. Identical factors are obtained at 42°C for (1) and 52°C for (2).

a photoconverter in gaseous media at atmospheric pressure and normal temperature in about the same spectral range as the TMAE vapour with a comparable quantum efficiency (QE). As shown in Fig. 1b, the fast RICH design now becomes extremely attractive: the pad cathode of the MWPC photon detector covered with such a CsI film, emits the photoelectrons isochronously, allowing for excellent timing properties [7]; the parallax error is governed only by the MWPC geometry; the chamber gap can be kept as thin as possible; the only window left is the one containing a gaseous or liquid radiator; a single gas can be circulated in the detector. In addition, in the proximity focusing case, a positively polarized electrode is added in the proximity gap to collect the ionization from minimum ionizing particles (MIP), keeping the MIP pattern spread as small as possible.

Following Seguinot's pioneering work on small area samples, the main remaining challenge, among others, is to demonstrate that large CsI photocathodes (PC) can be produced and operated in a detector with sufficient QE and good stability. What is understood by "sufficient QE" is illustrated in Fig. 2, which shows the TMAE temperature at which the fast RICH should be operated to obtain a factor of merit comparable to a CsI PC for a small fixed conversion gap (4 mm).

Such attractive features have triggered many groups to study the basic properties of CsI deposits and applications to HEP experiments, which will be discussed.

2. The CsI-RICH projects

We first present the experiments where a PID based on a CsI RICH is proposed. In Table 1, we indicate the main experimental parameters which will finally define the layout of the detector, such as separation, rates and charged multiplicities. The institutions where basic studies on CsI layers and/or RICH developments are being pursued in connection with these experiments are listed below Table 1.

The HADES Experiment [8] aims to study lepton pair production in collisions of Au ions of 1 GeV/N with a Au target up to a 1 MHz event rate and a multiplicity of 400 charged particles. Similarly to the CERES Experiment, the

Table 1
Some parameters of HEP experiments where PID using a CsI RICH is under consideration

Experiment	Machine	Particle target	Separation GeV/c π/K	Interaction rate (s^{-1})	Area detector (m^2)	Number of tracks in the detector	Radiator	Photon detector	Status
HADES	SIS/GSI	Au–FT	electrons	10^5–10^6	1.4	10–20	C_4F_{10}	MWPC	approved
HERA-B	HERA	p/FT	up to 60	10^7	8	200	C_4F_{10}	MWPC	proposed
ALICE	LHC	Pb–Pb	0.8–2.5	10^3–10^4	12	600	C_6F_{14}	MWPC	selected
NA44	SPS	Pb/FT	4–8	10^4–10^5	0.5	1–5	iC_4H_{10}	MWPC	operational
SMC/CHEOPS	SPS	μ-p/FT	10–150	10^5–10^6	6	20–40	CH_4/C_4F_{10}	MWPC	proposed
CDF	FERMI	p–p	up to 6	10^6–10^7	undef.		C_6F_{14}		proposed
PHENIX	RHIC	Au–Au	0.8–2.5	10^4	undef.		gaseous		proposed

HADES: Munich T.U.
HERA-B: Ljublijna Univ.
ALICE, CERN-RD26: Bari, CERN, EPF-Lausanne, Palaiseau, Saclay, Weizmann, Zagreb, Padova Univ., Giessen Univ.
SMC: CERN, Trieste, Bari.
CDF: Pennsylvania Univ., McGill Univ., Princeton Univ.
PHENIX: Princeton Univ., Stony Brook.
B-factory: College de France, Saclay, Palaiseau.

RICH is "hadron-blind" using a CH_4–C_4F_{10} gaseous radiator. The photodetector, being located at the back of the target, records only lepton rings of constant radii in order to give a fast decision on selected lepton pair events. A fast readout electronics [9] is under development which will provide the necessary hardware fast-ring-pattern-recognition algorithm. This apparatus should be operational in 1998.

At NA44-CERN, a novel imaging detector, called TIC for Threshold Imaging Cherenkov [10], aims to tag pions among kaons/protons in events of low multiplicity, magnetically selected in the 4 to 8 GeV/c momentum range from lead ion collisions on a lead target. Photons are radiated only by pions in the iC_4H_{10} radiator, permitting identification since K and p are below threshold (Fig. 3a). In the first version, the detector was operated with TMAE at 30°C using a wide conversion gap of 30 mm depth (Fig. 3b). Therefore, due to the proximity of the target, the photodetectors suffered from such a high level of charged particles background that their stability became problematic at high interaction rates. Replacing TMAE by CsI pad PCs enables the suppression of the collection of the ionization deposited in the conversion gap and the reduction of the sensitive gap to 4 mm and thus of the charged background by a factor of 8. This detector, the first Cherenkov imaging device operated with CsI PCs in an experiment, will provide valuable information on the long-term stability of large PCs under irradiation. The QE performance of these PCs will be quoted later.

The three fixed-target experiments, HERA-B [11], SMC [12] and HERMES [13], have in common a PID covering the 10–100 GeV/c momentum range. Focusing layout and gaseous radiators are foreseen, keeping the photodetectors well out of the region where charged particles are flowing by means of flat mirrors. The most advanced project, HERA-B, will have to cope with very high multiplicity and detection rate, up to 1 MHz/cm^2 at some locations, making the ageing capability of the photoconverter a crucial concern. TMAE and CsI versions are currently under study.

In fact, the CsI-fast RICH was initially proposed for PID at colliding B-factories [14]. Although the expected physics event rates and multiplicities are small, the requested particle separation, e.g. π/K at 3σ up to 4.5 GeV/c, is made very demanding by an incident angular range extending up to 60°. An important R&D programme was performed around Seguinot and Ypsilantis [15], leading to a large scale prototype, operated with TEA and CsI PC, and the production of a very fast digital integrated readout electronics [16]. Finally, given that the achievement of the required separation is questionable at large angles and also for other reasons, the techniques now selected at BaBar are based on the DIRC and aerogel [17] concepts. As mentioned earlier, a TEA-based fast RICH has been chosen at CLEO [5]. Very recently, a PID system using aerogel and HPD has been proposed at the LHC-B Experiment [18].

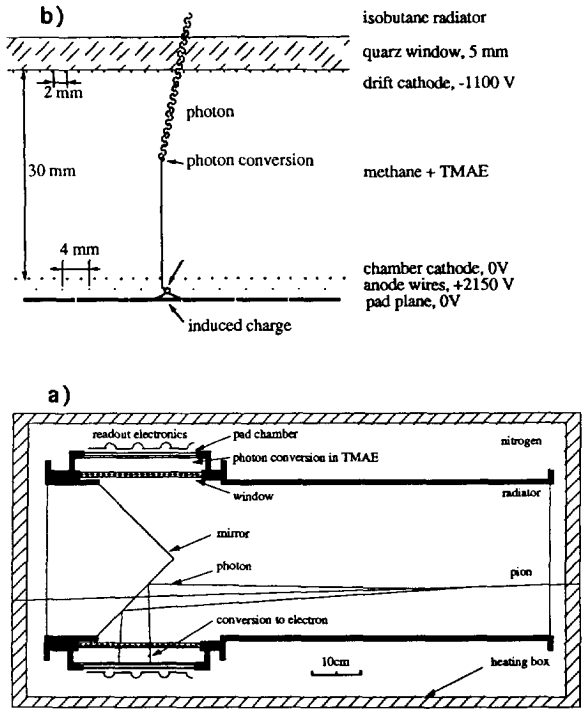

Fig. 3. (a) Side view of the NA44 Threshold Imaging Cherenkov (TIC) showing the 1 m long iC_4H_{10} radiator and the two photodetectors. An external set of pad MWPCs provide the 2-dimensional predictions of the tracks to define in the TIC the positions of fiducial disks (6 cm radius) where photoelectrons are expected (pions) or absent (kaon/proton). (b) Cross-section of a photodetector. When operated with TMAE, the drift cathode is negatively polarized to drift all charges, including background, created in the conversion gap in the MWPC. When operated with CsI evaporated on the pad plane, this drift cathode is positively polarized.

Specific requirements are found at the forthcoming experiments around heavy ion colliders, ALICE at LHC and PHENIX at RHIC, operating with Pb–Pb at 5.5 TeV/nucleon and Au–Au at 100 GeV/nucleon as centre-of-mass energies, respectively [19]. The physics is characterized by a very highly charged particle multiplicity, the p_t distributions of which peak at a low momentum value, e.g. 400 MeV/c for pions. At ALICE [20], a low event rate, $<$10 kHz for minimum-biased events, is expected, implying an irradiation dose smaller by several orders of magnitude than in the p–p operation mode. The PID requirement is first to complement the momentum ranges where the dE/dx identifications are not effective, that is in the 0.7–2.0 GeV/c range for π/K separation with gaseous detectors (TPC) and 100–200 MeV/c for lepton/π separation in solid state detectors. Secondly, a PID extended to momenta up to 3.5–5.0 GeV/c, is also considered for other specific physical goals. A particle density of 100 per m^2 is expected in a barrel of 3.5 m radius, meaning 150 m^2 of detector coverage for two units of pseudorapidity.

In the ALICE technical proposal [59], the present preferred scenario is to share the PID tasks between two detectors: a TOF counter barrel of 3.7 m radius for identification starting at the lowest momenta and, for high p_t hadronic separation, a CsI fast RICH wall at larger distance (≈4.7 m) and of smaller angular coverage (10 m^2).

At CDF [21], a detector upgrade for a future collider detector in B0 is under investigation. A PID for π/K separation in the 0.3–7 GeV/c range is the aim, also using a combination of TOF and a CsI fast RICH.

3. The CsI fast RICH

In a first section, devoted to the CsI problem, we discuss the efforts made to achieve the highest QE on large-area pad electrodes by developing the technique of the CsI film processing on an adequate substrate and demonstrate the stability of such PCs in time and with respect to irradiations. In the second section, we discuss how to produce a photodetector that has the highest single electron efficiency and a good performance in localization accuracy compatible with the expected rate and associated problems (photon feedback).

3.1. The CsI PC

3.1.1. Basics on CsI QE

During the past 3–4 years, considerable effort has been devoted to understand the intrinsic properties of CsI films operated under vacuum and gas. The reader is referred to the detailed review presented by Breskin on the subject at this workshop [22], containing an updated panorama of all results, problems and references related to CsI films. There will be only partial repetition of these here.

Basic studies are usually performed on small samples using UV monochromatic sources under optimum conditions of cleanliness and substrate surface and their control. Clearly, a very different situation will be found when a large area of PC has to be produced and inserted in a detector. For example, the PC substrate will be a printed circuit board (PCB) in order to fulfil the requirements of the photon detector. We shall compare the results obtained in laboratories with those obtained by a RICH detector.

The present status of the evaluation of the CsI QE is shown in Fig. 4 for measurements with UV lamps. Curves 2 and 3 were obtained in the context of the CERN-RD26 project [23]. They result from a large number of measurements performed by different institutes (Weizmann, Palaiseau, Saclay), involving stable CsI processing, treatment and calibration [24]. Within the limits of these procedures, which may not be fully optimized, the measurements are reproducible within ±5%. For this reason,

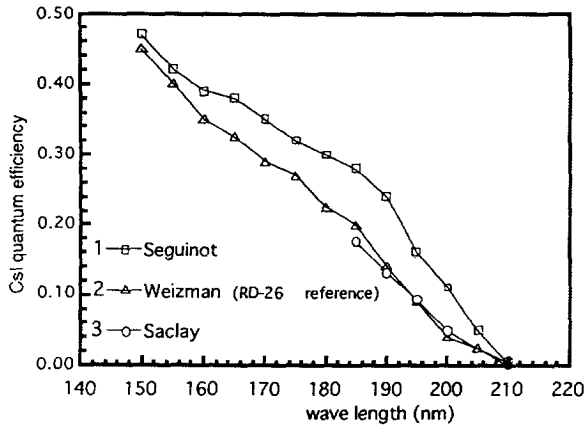

Fig. 4. Measurements of the CsI-QE made with monochromatic UV beams on small samples. (1) Seguinot et al. [6], best measurement. (2) Weizmann et al., curve averaging a large number of measurements. (3) The Saclay curve, measured in a MWPC.

curve 2 has been taken as a "reference QE curve" within our RD-26 collaboration. In fact, the first measurement published by Seguinot (curve 1 [6]) showed a significantly higher QE value, especially close to threshold. Even though this result was the best of a series of measurements, it suggests that an even higher QE than the so-called reference of Fig. 4 might be achievable and keeps the challenge opened for further studies.

3.1.2. CsI thin film evaporation

In the processing of CsI layers, some physical features of the CsI compound have to be taken into account. CsI is an insulator with poor thermal conductance, having a high vapour pressure at its melting point (0.1 mbar at 621°C). According to Maier-Komor [25], these features favour a dissociation of the CsI molecules during thermal evaporation when too high a temperature is reached at local points, an argument used by the above author to recommend the electron gun evaporation method using a cooled crucible and well-controlled surface evaporation. However, a large proportion of the users adopted the easier thermal evaporation. To palliate the above effects, the evaporation boat is prepared by pre-melting the CsI powder or small crystal pieces under vacuum, with the aim to obtain for the evaporation operation a good good thermal contact between the boat and its load. These remarks, supported by the observation of a non-stoichiometric composition of CsI thin films, indicate the need for further investigations (Section 3.1.4).

CsI is also known as a hygroscopic compound: when exposed to moist air, its surface becomes whitish. Many compounds are formed from reactions of water vapour with the CsI surface, such as cesium hydroxide (CsOH), oxide (Cs_2O), iodate ($CsIO_3$), and hydrogen iodide multi-

hydrate ($HI \cdot (nH_2)$). All of them will degrade the CsI QE by poisoning the surface and the CsI bulk after diffusion. In the case of free cesium, fast oxidation is observed. Therefore, the deposition of CsI film has to be performed in the best possible vacuum on a substrate free of moisture, requiring a heavy outgassing, preferably at the highest temperature tolerable by the substrate under vacuum.

The pre-molten CsI load is then evaporated on the substrate after a short release on a rotatable shutter at the beginning of the evaporation. At RD-26 [23], four boats are simultaneously evaporated, positioned so as to ensure a film thickness variation of not more than about 10% over an area of $80 \times 50\,cm^2$. That allows the distance from the sources to the substrate (50 cm) to be shortened, keeping the evaporation vessel small in size. The CsI loads are calculated so as to ensure the desired film thickness after complete evaporation of the four boats. The evaporation rate is controlled with quartz balances. No visible influence on the PC performance has been seen by varying the rate between 1 and 50 nm/s. In practice, the pressure during the evaporation in the different groups may range between 1.0×10^{-5} and 1.0×10^{-7} Torr without any clear indication of significant correlation with the PC performance. However, since the QE evaluation of a fresh PC is carried out just after its production, it is not impossible that all these early contaminants might influence the ageing properties of the film, affecting the rate of chemical reactions in the longer term.

When a large area of CsI film ($>1000\,cm^2$) is processed, it is observed that the initial pressure decreases during the evaporation, e.g. from 5.0 to 2.0×10^{-6} Torr, the initial value being restored after several tens of minutes. Such a pressure drop, of less amplitude, is also observed at lower initial pressure by Anderson, Breskin and Friese. The origin of this pressure drop is still unclear to us. It might be due to the blocking by the fresh layer of the substrate outgassing, but also to a reactive process between the residual gases (O_2, H_2O) and the CsI film under growth.

After some optional conditioning of the film that is done after evaporation, discussed in the next section, the vessel is vented with an inert gas (nitrogen or argon). Usually, when the fresh CsI PC is transferred to the detector, it is briefly exposed to air (10–20 min). It is known that such a short exposure will not significantly degrade the CsI performance. However, in order to check the possible influence on ageing, we can perform the transfer of the PC to the detector without exposure to air by protecting the PC in the evaporation vessel by means of a tight lid and by mounting the PC on the detector in a glove box.

3.1.3. Conditioning the CsI film by heat treatment

Up to now, all groups involved in the processing of CsI films have followed the above procedures, considered necessary but not yet firmly correlated to the PC performance. More controversial is the influence of the substrate and of the conditioning. The conditioning, initially described by Anderson [26], consists of heating the PC, kept under vacuum after the evaporation to 50–60°C for 4–6 hours. Breskin [27] made detailed studies in a setup allowing him to evaporate, heat and characterize the films in the same vessel. A drastic increase in the QE was observed, mainly in the long wavelength range (>190 nm), after heating the film to 60°C for at least 5 hours compared with measurements taken just after the evaporation. In addition, the films appear to have a better stability following exposure to air after conditioning. Such an effect was systematically reproduced by Breskin on a large number of samples, whatever the substrates, PCB included. However, as seen in the next section, when the heat treatment is applied to larger PCs made of PCB, such an improvement is more difficult to detect: generally the characterization of the fresh PC cannot be done in situ immediately after evaporation and the influence of the choice of the substrate and its conditioning still seem to dominate.

3.1.4. The substrate

Observations of films, done with the Scanning Electron Microscope (SEM) or higher-performance instruments like the Scanning Tunnelling (STM) or the Atomic Force (AFM) Microscopes indicate that the growth of a CsI film is initiated by a discontinuous germination of small islands, randomly spread over the substrate. While the evaporation is in progress, the film becomes continuous at a thickness of about 90 nm [28]. It is therefore made up of an aggregate of small cyrstallites separated by disordered grain boundaries. The mean size of these crystallites has been measured to be the largest (about 5–10 μm) on a quasi-perfect substrate like silicon [29]. Depending on the state of polishing of the substrate, that size can vary from 0.5 to several μm. X-ray diffractometry indicates that the grains are monocrystalline with preferential orientation [110]. As the growth is made at low temperature, it is probable that the shape of the grains is not the equilibrium one. It should be stressed that, for small grains, the film is composed of a large proportion of disordered crystals, implying that the electron transport properties are different from those of a perfect lattice [28]. Neither can such a structure be considered as a "specular" surface, as seen in Ref. [30], indicating a roughness of 20–40 nm.

More detailed information on the composition and the structure correlated to the primary and secondary electron emission of the films was obtained [30] using the Electron Spectroscopy for Chemical Analysis (ESCA) and the Photoemission Electron Miscroscope (PEEM) probes. These techniques provide a 2-dimensional mapping of the electron emission, with lateral accuracy down to 1 μm, leading to several important conclusions: (i) the stoi-

chiometry of the film is different from the expected 1/1 and is inhomogeneous at a scale close to that of the grain size; (ii) concurrently, the emission is also inhomogeneous, enhanced where iodine is in excess; (iii) ageing can lead to full segregation of CsI into iodine and cesium; (iv) reactive compounds, like I_2Cu which has a very poor emissive yield, are found when the substrate is made of copper.

Recently [22], the bulk and surface resistances of CsI thin film were measured, showing that the film is a rather poor insulator with a bulk resistivity of 10^{10}–10^{11} Ω cm.

3.1.5. Experimental results

Anderson et al. [31] obtained some of the highest QE values with pads etched on a PCB with copper cladding, using small pieces of CsI scintillator as evaporated material and conditioning the film at 65°C. At best, they achieved 0.29–0.31 at 180 nm and 0.22 as an average using a parallel plate chamber (PPC) filled with ethane at 20 Torr. TMAE vapour was taken as a reference to calibrate the photon flux.

Following this work, Hemmick et al. [32] used a pad substrate ($24 \times 20\ cm^2$) made of copper-clad PCB covered with a 800 nm thick layer of aluminium and oxidized by a long exposure to air. The heat treatment was performed at 52°C after transfer (through air) of the PC to the detector. Using a PM as photon calibration, they measured a QE of 0.20 at 180 nm. There is no evidence that the heat treatment is responsible for this high value since the initial QE is not quoted. After this calibration, the PC was mounted on a focusing RICH with a gaseous radiator (CH_4, C_2H_6). The photodetector was a PPC filled with ethane at 20 Torr. Analyzing the measurements obtained from Cherenkov light emitted by 1 GeV/c particles, they obtained photon yields corresponding to 62–88% of those expected from the QE calibration measurement. This loss is attributed to unknown attenuation in the radiator and to possible lower QE.

In turn, Lu et al. [33] found that the best QE was achieved on aluminium substrates in comparison to Au, Cu and Sn/Pb. A value of 0.25 was measured at 180 nm with a UV lamp and small samples, dropping to 0.15 when evaluated in the detector. The positive influence of aluminium coating on copper was also observed, although followed by a QE drop of 10–20% after several days. There is no mention of any heat treatment. The Cherenkov test of this PC ($16 \times 16\ cm^2$), performed with a MWPC filled with ethane at atmospheric pressure and a C_6F_{14} radiator, led to a QE value of 90% of the UV lamp result.

Kononenko et al. [34] presented the results of a systematic study of a large variety of substrates and treatments, also using a PPC filled with iC_4H_{10} at 20 Torr. They compared substrates made of Cu, Ni, Ag, Au, Cr, Sn/Pb and Al with a UV-lamp. The highest QE was found on Al (0.14) and the lowest on Pb/Sn (0.07) at 190 nm. Ceramic pad planes were also investigated and found to behave identically to the others. Fine polishing and careful cleaning of substrates did not appear to have any positive influence, nor heat treatment (only 2–3 hours at 60°C after evaporation). A comparable QE was measured in Cherenkov mode.

Seguinot et al. [35] followed a very careful procedure in the elaboration of their pad substrates of size $42 \times 15\ cm^2$. The pads were covered with a thick electroplated gold layer, preventing any contact with underlying copper. A thin layer of gold was first evaporated, necessitating an appropriate mask to avoid electrical short circuits between pads, and the CsI was deposited in the same vacuum on the "fresh" gold layer using the same multi-source evaporation stand as RD26. The PCs were heated under vacuum before evaporation and transferred to the detector after a short exposure to air. No heating post-treatment was performed. Connected to a thin gap MWPC (0.50 mm), the fast digital electronics ($T_{integ} = 20$ ns) in use in the RICH tests imposes operation at high gain in order to achieve full single-electron detection efficiency, which is obtained in case of TEA operation [15] as well as with CsI films of 50 nm thickness, of low QE (0.07 at 180 nm). It was observed that thicker films provoked dark current, leading to discharges in the presence of a beam. QE evaluations were obtained by extrapolating values measured at reduced gain. The QE of films deposited from crystalline CsI was found to be 30% higher than for those made of CsI powder, corroborating previous observations by Anderson [31]. Operating at a temperature of 48°C increases the QE by 68%. The best result achieved was a QE of 0.14–0.16 at a 100 nm thick CsI crystal and 48°C. A significant loss (factor 2) in QE was observed over a 2 month period, attributable to the poor quality of iC_4H_{10} used in some of the tests. This loss was negligible with a methane/n-hexane mixture.

Krizan et al. [36] obtained the best results ever measured with a UV lamp, 0.30–0.35 at 180 nm, on substrates made of copper-clad PCB covered with the Sn/Pb alloy used for soldering; this value was reduced by 60% on a copper substrate. Their RICH tests were first performed with a Sr source and a NaF radiator, then [37], using an argon radiator and a MWPC geometry similar to that of Seguinot (0.62 mm gap) equipped with digital electronics. The PCs were submitted to a preliminary fine polishing and the heat treatment was applied after evaporation. In these tests, a loss in QE of 50 to 80% was observed, corresponding to a QE value of 0.17–0.26 at 180 nm.

Friese et al., at HADES, evaporated the CsI with an electron gun on standard copper-clad PCB, chemically covered with gold. A RICH prototype of size $50 \times 50\ cm^2$ was built and tested at an ion beam at GSI/Darmstadt [38]. The MWPC has a 1.5 mm gap and is equipped with analog electronics (Amplex and Gassiplex). A QE of 0.08–0.10 at 180 nm was measured, a low value attributable to damages which have occurred during the processing of the PC.

At Saclay, Besson et al. [39] also investigated a variety of substrates, Cu, Au, aluminized mylar, Al, Cu/Ni, using a MWPC and a pulsed Nitrogen lamp. They did not apply the heat treatment, which was found to have little effect in any of their tests. The best results, 0.20 at 180 nm, were obtained with the Ni/Au substrate. Recently, a new substrate covered with sprayed carbon was also tried, giving a higher result (0.26). The same PCs were tested in a RICH of size $10 \times 10\,cm^2$, flushed with methane and with solid or liquid radiators, achieving about the same QE performance.

At CERN (RD-26), all of our QE measurements were done with a RICH, the samples being measured with a UV lamp at the Weizmann Institute. In a first period, ten PCs of size $30 \times 30\,cm^2$ were produced. The substrate was made of a standard copper-clad PCB, G10, chemically covered with gold with a coarse surface state. Evaporations were carried out repeatedly on the same pad substrate after removing the previous film by washing it out with water/alcohol and baking at 60°C. Various tests were made relating to the evaporation procedure: powder vs crystalline CsI, rate, thickness, temperature of the substrate, etc. All these tests provided a QE value about 0.07–0.10 at 180 nm [40]. Then, an extensive study of the morphology and the structure of the films was carried out at RD-26, the results of which are mentioned in the previous section [29]. They led us to develop a substrate of much better surface quality according to the following procedure. The pad pattern is first etched on the copper-clad G10. A fine polishing is done with alumina paste, the cleaning of which is not easy but essential. This mechanical polishing is followed by a chemical polishing. Precautions should be taken to make the traces on the PCB thick enough so that they do not disappear during the chemical polishing. Then a layer of nickel, 7 μm thick, is chemically deposited, followed by a thinner (0.5 μm) layer of gold. The resulting substrate is now much brighter and all scratches are absent. Six new PCs of sizes 30×30 and $80 \times 25\,cm^2$ were fabricated, each with its own pad substrate. A better QE was observed [41], now ranging from 0.13 to 0.19 at 180 nm. The largest values were obtained on four PCs submitted to a more prolongated heat treatment (60°C for 12 hours after evaporation, under vacuum). However, it is not clear whether this improvement is attributable to only one of the two new procedures, polishing or long heat treatment, since they were performed together. More details on these measurements can be found in Sections 5 and 6.

All the results obtained with UV-lamps and RICH detectors are summarized in Fig. 5. At this point, it is premature to draw any statistical conclusion from these QE measurements since in some cases it is still difficult to disentangle the influence of different sources of errors uncorrelated with the basic CsI-QE. However, several features have been found to be reproducible by all the investigators:

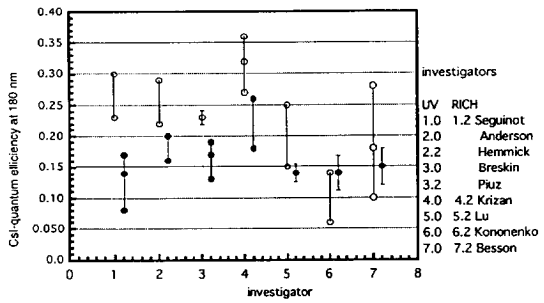

Fig. 5. Summary of the CsI-QE measurements at 180 nm obtained with UV lamps (open circles) and RICH tests (filled circles).

(i) UV lamp measurements: a QE of around 0.24 is achieved by most groups, except by Kononenko et al., significantly higher results, up to 0.30–0.35, are repeated by a few other groups;

(ii) in all RICH measurements using a liquid/solid radiator, the QE value is found to drop almost uniformly by some 30% to around 0.17;

(iii) when UV and RICH tests are done with the same chamber, they give comparable QE evaluation (Besson, Kononenko, Lu).

High values are also observed in RICH tests and, coincidently, both when the photons are generated by a gaseous radiator and a Sr source, questioning the influence of the incident angle at the PC surface. Mine et al. [42] have recently evaluated the influence of the incident angle up to 60° with non-polarized photons and a small sample. They observed a QE drop which increased with the photon wavelength, 30% at 60°. It might be of interest to crosscheck this measurement with a RICH setup and polarized photon beams. Finally, as unanimously pointed out, the largest differences are obtained between UV measurements performed in a very clean metallic setup and MWPCs partly composed of outgassing materials.

3.2. The photodetector

3.2.1. Geometry of the photodetector

The photodetector has to locate as efficiently and accurately as possible single electrons emitted by the CsI deposited on the pads which are the only elements to be instrumented with electronics. In the case of single electrons, very small signals have the highest probability of being generated due to the expected exponential pulse height (PH) distribution, the small avalanche size and the loss due to the anode/cathode coupling. Increasing the chamber gain to moderate this situation unfortunately has several limitations. The first is related to ageing since the impact on the PC of the ion clouds produced from each avalanche is the main source of degradation of the CsI film. Discharges, initiated by charging up the CsI, could possibly occur at very high local irradiation rates even if CsI is proven to be a poor insulator. The second limitation

is imposed by the photon feedback (PF) mechanism. The primary avalanche isotropically emits photons, which can in turn re-emit single electrons by hitting the CsI PC. Their number is taken to be proportional to the total avalanche charge Q_0, that is the chamber gain G in case of a single electron, according to $N_{pf} = K_{pf}G$ [43]. Such a feedback can diverge at too high a gain and is also responsible for a background uncorrelated to the Cherenkov candidates.

Therefore, a natural choice is to keep the anode/pad gap as small as possible in accordance with the pad size and the integrating time, T_{integ}, of the front-end electronics. In turn, the driving parameters are the local particle rate to be sustained, the method used for coordinate determination by analog or digital barycentre calculations, and the limitation of the number of pad channels. Their relative implications can be enumerated as follows:

– a very high rate (p–p LHC) implies T_{integ} less than 50 ns, hence a small signal requiring a small gap for a maximum anode/cathode coupling;

– a small gap (<1 mm) calls for a digital readout since the pad size will be too small, and the number of pads too high for efficient analog barycentre findings;

– a medium rate (a few hundred kHz) allows for longer T_{integ}, up to 500–600 ns. Thanks to the larger signal, the gap can be increased to permit analog barycentre finding with pads of 50–100 mm^2, even though the geometry is not optimized for the best accuracy of that method (pad width≈gap).

3.2.2. Gain and induction spread

In a MWPC geometry, shown in Fig. 6, a single electron extracted at the abcissa x of the cathode 1, generates an avalanche of charge Q_0 concentrated, in the case of low gain, at a point of the sense wire defined by the angle α (tg $\alpha = \tanh(\pi l/s)\mathrm{cotg}(\pi x/s)$). In the motion of Q_0 towards the cathode 1 during a time t, the charges $q_-(t)$, $q_{+1}(t)$, $q_{+2}(t)$ are induced on the sense wire, cathode 1 and 2, respectively. According to Va'vra's nomenclature [44],

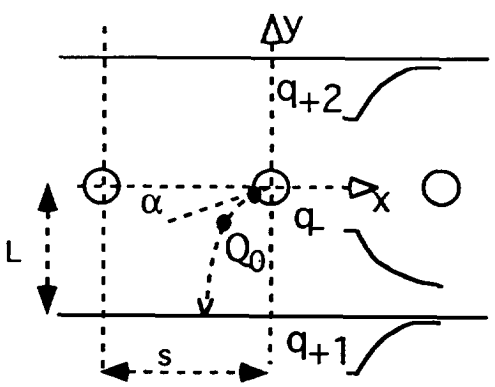

Fig. 6. Schematic of the motion in a MWPC of the positive charge Q_0 and the resulting induced charges.

these quantities are referred to as "visible gain" when measured at T_{integ}, while Q_0 is the total gain reached when T_{integ} equals the total ion drift time, (>10 μs). In order to evaluate the photon feedback yield, Q_0 must be deduced from q_{+1} measured at T_{integ}.

For that purpose, a first correction factor for $q_-(T_{integ})$ is obtained from the equation of motion of Q_0 in the MWPC field structure, assuming a known constant ion mobility, $\mu = v_+/E$. An example of such a curve is shown in Fig. 7 for the case of methane, indicating an increase by a factor of approximately 2 in signal amplitude between $T_{integ} = 20$ and 600 ns for the same gap. A second correction factor takes into account the fraction q_{+1}/q_- of the charge induced on the pad cathode. When the gap is small, this factor depends on the angle α, that is, on the location of the electron emission. Seguinot [45] has measured a 15% variation for a 0.67 mm gap, which is the order of magnitude of the error expected when determining Q_0 by measuring $q_{+1}(t)$ without knowing the location. However, the spatial extension of Q_0, assumed to be punctual in the calculation, should reduce the spread $q_+(t)/Q_0$.

For a given MWPC geometry, different models [46] provide the parametrization of the geometrical spread of the induction as a 1-dimensional projection in a plane parallel to the sense wires. In turn, the 2-dimensional spread, necessary in the case of a pad array, can be generated by a revolution of the 1-dimensional curve around an axis, an approximation which does not take into account the field periodicity in a direction perpendicular to the anodes. Since such a shape is ultimately convoluted with experimental fluctuations such as electronic noise, it is possible to use a Gaussian profile, the variance of which is obtained from a dedicated measurement as seen in Fig. 8.

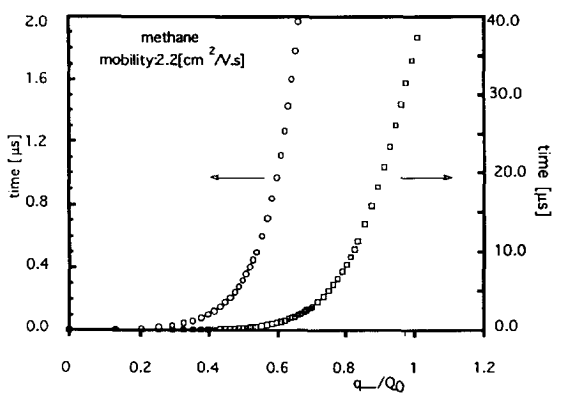

Fig. 7. Time dependence of the ratio of $q_-(t)$, the charge induced at the anode, to the total charge Q_0 moving towards the cathode, calculated in methane for $x = 0$ (see Fig. 5). The plot on the right shows $q_-(t)/Q_0$ until Q_0 reaches the cathode (at $T_{integ} = 40$ μs); on the left, one sees the fraction of Q_0 measured for $T_{integ} <$ 2000 ns.

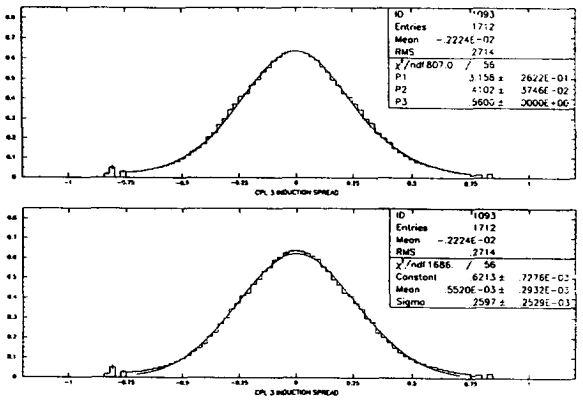

Fig. 8. Spread of the induction in a MWPC with 3 mm gap, 4 mm pitch, 20 μm anode diameter (x-unit in cm). The measurement is fitted with the Gatti model in (a) and with a Gaussian in (b).

3.2.3. MWPC gas mixtures and Cherenkov radiator media

The gas mixture has to have the best UV transparency relative to the CsI threshold. The most commonly used gases are CH_4, C_2H_6, iC_4H_{10}, and the mixtures they form with Ar and He. To minimize the photon feedback yield and improve the stability, a well quenched mixture is desirable, meaning some admixture of iC_4H_{10} or neopentane. On the other hand, it has been demonstrated that the photoelectric yield of a CsI PC depends on the gas species via the parameter E/p where E is the electrical field strength at the surface of the PC and p the pressure. A study [47] has shown that the elastic cross section of the gas is responsible for the backscattering of a proportion of the photoelectrons, conversely reducing the apparent CsI QE. This model is in good agreement with recent measurements performed with a laboratory cell [48] and a RICH detector [41]. The same QE is found in vacuum and pure CH_4 at atmospheric pressure when $E/p > 2$ V/cm · Torr. With mixtures composed of CH_4, iC_4H_{10} and argon, the yield drops by about 10–20% up to 100% in a He-based mixture. This effect is considerable when a MWPC is used, where the electrical field strength is low at the cathode surface (≈1–2 kV/cm), another good reason for decreasing the gap. The use of a noble-gas-based mixture, of potential interest in order to reduce the total load of flammable gas for a very large system, also implies an increase in the photon feedback yield [41].

For PID at momenta larger than 15 GeV/c, the gaseous radiators used are typically C_4F_{10}, C_5F_{12}, CF_4, CH_4, noble gas, etc. while, at lower momenta, solid or liquid media are necessary. In the case of fully gaseous media, the separating window can be made of quartz or, if the gaseous UV transparencies are good enough, a CaF_2 window (if affordable) enables advantage to be taken of the higher CsI QE at shorter wavelengths. The best liquid radiator is C_6F_{14}, the UV transparency of which matches the one of a containing window made of quartz. The low refractive index and the low chromaticity of this liquid make it attractive in comparison to the solid media (NaI, LiF, CaF_2) of highest transparency. Users should be warned that the internal stresses of such crystals, if not completely annealed, may locally affect their transparency to polarized Cherenkov photons.

3.2.4. Mechanics and electronics

3.2.4.1. The pad CsI cathode panel. As soon as large area PCs are envisaged, their design has to be adapted to the usual MWPC constraints, and ultimately to cost-effective solutions. In all developments under way, the 2-dimensional readout requires that the cathode is segmented into a pad array, of size ranging from 30 to about 100 mm^2. In turn, such a size necessitates locating the front-end pad electronics at the back of the cathode plane. Finally, the usual flatness requirement, gap width dependent, (±20–50 μm) determines the technology used to assemble the electrode.

Two examples are shown in Fig. 9 both using PCBs. One (Fig. 9a), developed by Seguinot [16] for their large prototype, is adapted to a high bandwidth electronics requiring minimum length of connection between the pad and the front-end amplifier: the electronic board is directly plugged into the pad PCB of suitable thickness (2.4 mm). The PCB (multilayer) is designed such that there are no

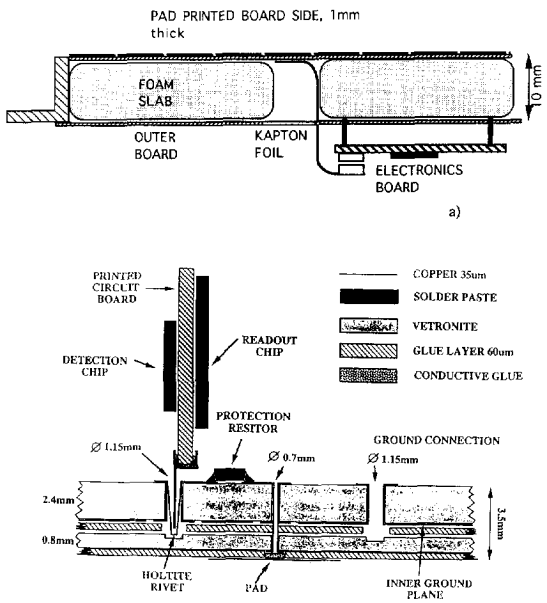

Fig. 9. Cross-section of pad electrodes to be covered with CsI and equipped with front-end electronics. (a) Composite panel for large area. (b) Technology suited to fast electronics [15].

traversing holes and the pad can be electroplated with gold. It is glued onto a metallic frame ensuring flatness and stiffness. Panels of size $20 \times 80\ \mathrm{cm}^2$ were produced. The second example, used by the CERN-RD-26 group, is based on the classical "composite panel" technology as shown in Fig. 9b. The pad PCB, described in Section 3.1.5, is a thin double-layer circuit (0.8 mm), fabricated so that the connection to the pads is made via non-traversing holes. Thin kapton foils, grouping 48 pads, are soldered onto the opposite side of the pads. A cathode panel is made by glueing together the pad PCB, a foam plate and another thin PCB into a metallic frame. The total amount of material, including the front-end electronics chips and board, is equivalent to 3% of a radiation length. A large-area stiff light panel can be achieved with this technology by increasing the thickness of the massless foam.

In order to be coated with CsI, the pad panel has to be placed in a good vacuum and withstand a certain temperature for the heat treatment, as seen before. A flat cover can be fixed tightly on the metallic frame enabling the rear of the panel, where all the outgassing components, connectors, electronics, foam, etc., are located, to be insulated by pumping it separately, avoiding too long an outgassing.

3.2.4.2. Electronics. Currently, two ASIC-VLSI electronics systems, specifically designed to be installed on arrays of large pads, are available. The first is a digital system designed by Seguinot et al. [16] to cope with the event rate expected at LHC. It is composed of two chips: a front-end one (8 preamplifiers and comparators) and a logic one permitting fast serial/parallel readout with zero suppression (3 μs/1024 channels). A second version is in preparation with an improved signal/noise performance. The second system, AMPLEX [49], permits an analog multiplexed readout when connected to a CAMAC module performing the digitization and zero suppression. This chip is now available in a new version, GASSIPLEX [50], specifically matched to the MWPC current pulse shape and having an upgraded baseline restoration. This circuit will be the analog front-end part of DIGITPLEX [51], under design for ALICE, where an ADC on chip allows 8 bit digitization and zero suppression of 16 channels within 3 μs.

Most of the results presented here were performed with RAL, AMPLEX and GASSIPLEX electronics.

4. QE measurement with a RICH

The performance of the detector is characterized by N_0, the factor of merit which allows N_{phel}, the number of photoelectrons per ring, to be evaluated according to:

$$N_{\mathrm{phel}} = \varepsilon_{\mathrm{det}} \varepsilon_{\mathrm{tr}} N_{\mathrm{ph}} ,$$

where N_{ph}, the number of photons per ring, is given by

$$N_{\mathrm{ph}} = L_0 (\sin^2\theta) N_0 ,$$

with

$$N_0 = 370 \int \prod_i (\mathrm{tr}_i(E)) \prod_i (\mathrm{ref}_i(E)) \mathrm{QE}(E)\, \mathrm{d}E$$

and

$$\cos\theta = 1/\beta n(E) , \tag{1}$$

where β is the particle velocity, E the photon energy, $n(E)$ the refractive index of the radiator medium, L_0 the radiator length, and tr_i and ref_i the transmission and reflexion photon-loss coefficients through the detector media. The geometrical photon-loss through the grids, $\varepsilon_{\mathrm{tr}}$, and the single electron detection efficiency, $\varepsilon_{\mathrm{det}}$, are both photon-energy independent.

Evaluation of the unknown QE(E) can be done in the experimental configuration under study provided that all sources of secondary photon emission are correctly parameterized, which requires in fact, measurements complementing the Cherenkov photon yield.

The raw data of a Cherenkov ring are provided by the detector as a two-dimensional pad pattern, possibly with analog information. Extracting N_{phel} from such patterns is done by comparing data to a Monte Carlo simulation.

4.1. The Monte Carlo simulation

We list below the sequence of operations necessary to generate the pad pattern associated with a Cherenkov ring.

(i) Generation of the Cherenkov electrons according to Eq. (1):

- emission of Cherenkov photons from a particle of momentum p travelling through a radiator of index $n(E)$, along a path of length L_0;
- calculation of the losses by transmission and reflection in the detector media and through grids of the p-polarized photons during their transport to the PC;
- loss by reflexion of the p-polarized Cherenkov photons on the CsI film;
- extraction of single electrons at known locations (x, y) of the pad array, according to an arbitrary QE(E) characteristic, $\mathrm{QE}_{\mathrm{test}}(E)$.

(ii) Generation of the primary pad pattern of a ring.

- Choice of a single electron charge (or pulse height) generator: the more general one is a normalized Polya generator [52] characterized by two parameters, q_0 and θ, according to

$$P(q) = \frac{1+\theta}{q_0 \Gamma(1+\theta)} \left(\frac{q}{q_0}(1+\theta)\right)^{\theta} \exp\left(-\frac{q}{q_0}(1+\theta)\right) ,$$

$$0 < \theta < 1 ,$$

$$P(q) = \frac{(1+\theta)^2}{q_0 \Gamma(2+\theta)} \left(\frac{q}{q_0}(1+\theta)\right)^{\theta} \exp\left(-\frac{q}{q_0}(1+\theta)\right) \quad -1 < \theta < 0 . \tag{2}$$

The variable q can be taken as the induced charge or the pad pulse height measured at the time T_{integ}, of mean q_0 or PH_0, respectively. The factor converting the PH unit (usually an ADC bin) into a charge unit (fC) is obtained by an electronic calibration. The choice of the parameter θ is discussed in the next section. In the case of low amplification, a simple exponential generator can be used:

$$P(q) = \frac{1}{q_0} \exp\left(\frac{-q}{q_0}\right) . \tag{3}$$

- Choice of a function parametrizing the geometrical 2-dimensional spread of the induction: referred to as SPREAD(x, y) (see Section 3.2.2).

Then, for every photoelectron (i) extracted at the location (x_i, y_i), the generator provides a value $q(i)$. This total charge is shared between one or more pads according to SPREAD(x, y) to generate a primary pad cluster. All these clusters are overlapped by summing all PH(i) to form the primary PH ring pattern. New clusters, defined as local arrays grouping pads with adjacent edges only, are created and referred to as raw clusters.

(iii) Generation of the total pad hit pattern (photon feedback and electronic noise):

- Feedback photons are emitted isotropically from the location of the avalanche at the sense wire. Their number is taken to be proportional to the total avalanche charge Q_0, that is the chamber gain G in the case of a single electron, according to $N_{\text{pf}} = K_{\text{pf}} G$ (4). Seguinot [43] gives a value of $K_{\text{pf}} = 7.7 \times 10^{-6}$ in hydrocarboned mixtures based on photonic emission of three de-excitation lines of atomic C.
- The $Q(i)$ associated with every $q(i)$, the ratio $R_q = q_+/Q_0$ must be tabulated with respect to the position x for the MWPC geometry, the ion mobility and the time T_{integ} being used.
- For these feedback photons converted into photoelectrons at the PC, pad clusters are generated. This process is iteratively repeated until no feedback photons remain.
- These pad PH patterns are overlapped with the primary pattern together with a random electronic noise generator to provide the final event pad pattern.
- Finally, all the PH(i) are compared with an electronic threshold TH(i) and only pads satisfying PH(i) > TH(i) are kept. In an analog system, the TH(i) are obtained by measuring pedestal distributions of mean PED(i) and rms SIG(i) and defined as TH(i) = PED(i) + $N \times$ SIG(i), N being an adjustable constant.

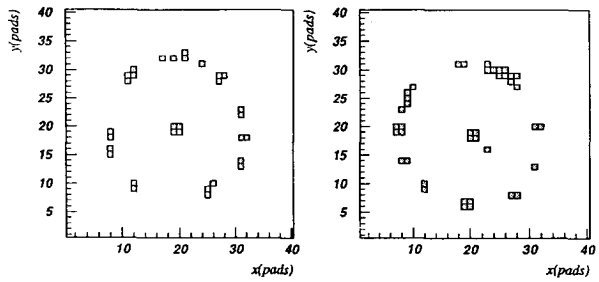

Fig. 10. Single events of Cherenkov rings obtained at RD-26 (PC19) using 10 mm C_6F_{14} thickness, 2070 V and CH_4. At the centre, the pad pattern of the incoming 3 GeV/c pion can be seen. The pad size is 8×8 mm^2.

This comparison provides the final hit pad patterns to be compared with the experimental ones.

It should be noted that the thresholding operation made on a discrete pad array introduces a bias to the initial PH generator: it may suppress a large proportion of the generated total PH when small values, two or three times the threshold value, are shared by several pads. Such a cut is found to affect the shape of the resulting distribution in the low PH range, where a genuine Polya bending is expected.

4.2. The pad pattern recognition and the total number of electrons per ring

Examples of single rings shown in Fig. 10 illustrate the pad patterns as measured at the test beam. An unambiguous recognition of every Cherenkov electron is made difficult because of primary clusters overlap. The expected fraction of geometrical overlap due to the number of Cherenkov photons along a ring is shown in Fig. 11 as a function of the ring radius. These fractions, for example

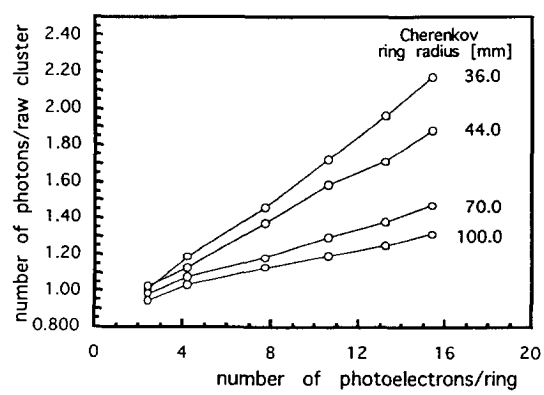

Fig. 11. Illustration of the pad pattern overlap probability in a MWPC geometry of 2 mm gap, 4 mm pitch, 8×8 m^2 pad size as a function of the number of photoelectrons per ring and for different ring radii.

1.2 photon per raw cluster for 100 mm ring radius and 15 photon per ring, are found to be large due to the geometry under consideration (2 mm gap, pad size $8 \times 8\ mm^2$), which is necessary for analog measurements. A smaller gap makes these fractions smaller [15].

The analog information makes possible the application of simple algorithms [40] to recognize single electron patterns and to deconvolute raw clusters into two or more single electrons. They are based on the comparison of the distribution of charge between the pads forming a cluster and SPREAD(x, y), allowing classifation of topologies into clusters of 1, 2 or 3 electrons. "Raw" clusters can be deconvoluted into "resolved" clusters. However, this method is limited by the fraction of single pad events. In the case of large pad size, this fraction is as large as about 40–60% which makes the deconvolution mathematically inapplicable. Therefore, this method will only provide us with a mean number of "resolved" clusters per ring and the number of electrons can only be statistically evaluated, by multiplying by a coefficient obtained from Fig. 11.

A Cherenkov fiducial zone can be associated with every particle of known position and velocity. The boundaries of this zone are defined by the RICH geometry and the photon wavelength range. The division of the sum of the whole PHs within the zone by PH_0, the mean of a single electron PH distribution, provides the number of electrons extracted in this fiducial zone. This number is the sum of actual Cherenkov photoelectrons and some of their associated feedback photoelectrons. Assuming that PH_0 and K_{pf} are known, this method provides another way than counting clusters to obtain N_{phel}. The evaluation of PH_0 and K_{pf} will be discussed in Section 5.

4.3. Evaluation of the QE characteristic

All of the chromatic information associated with every photoelectron is lost when measuring quantities like N_{phel} within a fiducial zone. Therefore comparison of these quantities with the simulated ones will only validate the integral of the $QE_{test}(E)$ curve. The fit can be optimized by applying scaling or shaping operations to this curve.

When using a C_6F_{14} radiator, it is difficult to determine the wavelength of the photon associated with a single electron for two reasons: the low chromaticity of this liquid requires a high electron localization accuracy and the unknown emission position of the photon inside the radiator leads to large geometrical error (unless the radiator thickness is reduced to a few mm). It will be seen in Section 6 that some information on the wavelength dependence of the QE can still be estimated by comparing measurements at different radiator thicknesses.

Alternatively, one can take advantage of a highly dispersive solid radiator like NaF or CaF_2 using large enough Cherenkov radii to measure the wavelength dependence of the QE in a RICH, or the differential QE curve. In this case, the fiducial zone is segmented into smaller zones, each corresponding to a sufficiently narrow wavelength interval. As seen in Ref. [41], the photoelectron localization accuracy is sufficient to count them in sequential zones equivalent to a 0.2 eV width, using a 10 mm thick NaF radiator and 100 mm Cherenkov radius, and thus derive the differential QE. Such measurements [41] should be repeated with a thinner radiator.

5. Single electron detection

5.1. Modeling

A basic feature for characterizing a RICH is the single electron pulse-height distribution, SEPHD, and its mean, PH_0. This feature permits the evaluation of the single electron (SE) detection efficiency. As seen in Section 4.2, an accurate value for PH_0 is necessary for evaluating N_{phel}, the number of photoelectrons per ring. The shape of the SEPHD reveals other features, such as the quenching property of the gas mixture and the fraction of feedback photons.

The shape of the SEPHD is usually found to be a purely exponential Furry distribution at low gas amplification whatever the gas mixture. Increasing the gas gain modifies the Furry into a Polya-shaped distribution, the curvature of which depends on the gas mixture used (see Eqs. (2)). Mixtures exclusively composed of hydrocarboned gases (CH_4, C_2H_6, iC_4H_{10}) lead to a concave shape, associated with a positive θ value. It is observed that a convex shape, associated with a negative θ value, characterizes a poor quenching property, typical of noble-gas-based mixtures (argon, helium). It has been suggested [53] that the θ constant is related to the Fano factor, according to $F = 1/(1+\theta)$: the lower the Fano factor, the lower the avalanche size fluctuation [54].

In addition to the generation of secondary electrons from the primary avalanche in poorly-quenched mixtures, secondary electrons are also produced by feedback photons in the case of CsI coating. For CH_4, the yield of photoelectrons per avalanche is expected to be 10–40% according to Eq. (4), taking $K_{pf} = 7.7 \times 10^{-6}$, $G = 2\text{–}4 \times 10^5$, QE = 0.2–0.3, percentage of the solid angle = 0.3–0.4. Mixing events composed of one or two photoelectrons modifies an exponential SEPHD into a curve which can also be fitted by a Polya function with a positive θ (concave shape). However, when measured with a pad array, that shape is still modified by the thresholding bias (Section 4.1) and the Polya shape inherent to the gas mixture and chamber gain in use.

An exhaustive survey of the response of pad detectors to a single electron can be found in Va'vra's report [44] presented at this workshop. It can be seen that many SEPHD obtained in hydrocarboned gases show an excess of counts at high PH values respective to an exponential SEPHD, which can be fitted with a Polya curve with

negative θ. To obtain such a convex Polya shape from a simulation, one has to take the number of secondary electrons per event to be larger than one. In fact, the Polya fit becomes poor since the resulting distribution is more a convolution of an exponential with a Landau-like distribution than a genuine Polya.

5.2. Experimental results with and without CsI

5.2.1. SEPHD obtained from a RICH

The cleanest way to measure a SEPHD with a RICH is to use a large enough Cherenkov radius (100 mm) and a thin radiator, 1 or 2 mm in order to minimize the overlapping frequency due to a small number of clusters per ring. Pad clusters are selected to correspond to single electrons. However, it is difficult to eliminate those clusters where an additional feedback photoelectron overlaps with the primary one. Therefore, such a SEPHD may be expected to yield too high a PH_0. An example is shown below.

5.2.2. Evaluation of the photon feedback yield, K_{pf}

We present the preliminary results of a method allowing measurement of the yield K_{pf} in any gas mixture. The method is currently applied to check the value proposed by Seguinot in hydrocarboned mixtures.

For this purpose, a pad cathode was half covered with CsI and photoelectrons were extracted using a well collimated UV source (deuterium lamp) from two distant spots, one covered and one not covered with CsI and the resulting SEPHDs were compared. The two spots are located along the same sense wire, used as a trigger for the pad electronics in both cases. Measurements were obtained using a MWPC with a pad size of $8 \times 8\ mm^2$, 2 mm distance from anode to cathode, 4 mm pitch and CH_4, iC_4H_{10}/CH_4, Ar/CH_4 as gas mixtures.

The SEPHDs measured at the two spots are compared for different voltages in Fig. 12. Without CsI coverage, the distributions have positive θ values increasing with the chamber gain, while the corresponding θ values are negative at the spot with CsI. To simulate these measurements, by varying K_{pf}, a proportion of photon feedback photons is added to a primary SEPH generator obtained from the fit of the no-CsI SEPHDs until the θ value measured at the CsI spot is reproduced. The total gain $Q(i)$ is calculated from the measured PH(i) as $Q(i) = k_1k_2k_3\mathrm{PH}(i)$ where $k_1 = 2.0$, $k_2 = 2.1$, $k_3 = 0.385$ fC/ADC bin represent the proportion of the charge at $T_{integ} = 700$ ns, the mean anode/cathode coupling and the electronics sensitivity, respectively. These factors translate the K_{pf} value of 7.7×10^{-6} [electron^{-1}] into $K'_{pf} = 0.078$ [ADC bin^{-1}], used in the following plots.

The measured and simulated θ values are compared in Fig. 13: the measurement is in agreement with the value proposed by Seguinot in CH_4 only at a gain $\leq 2 \times 10^5$. As seen in Fig. 12, for higher gain, the SEPHDs measured with CsI shows a shoulder at high PH (>300 ADC bin). The simulation reproduces this shoulder, which is due to the fraction of events where the total number of electrons become high enough ($\geq$5 per event) to make apparent their Landau-like distribution, convoluted to the genuine

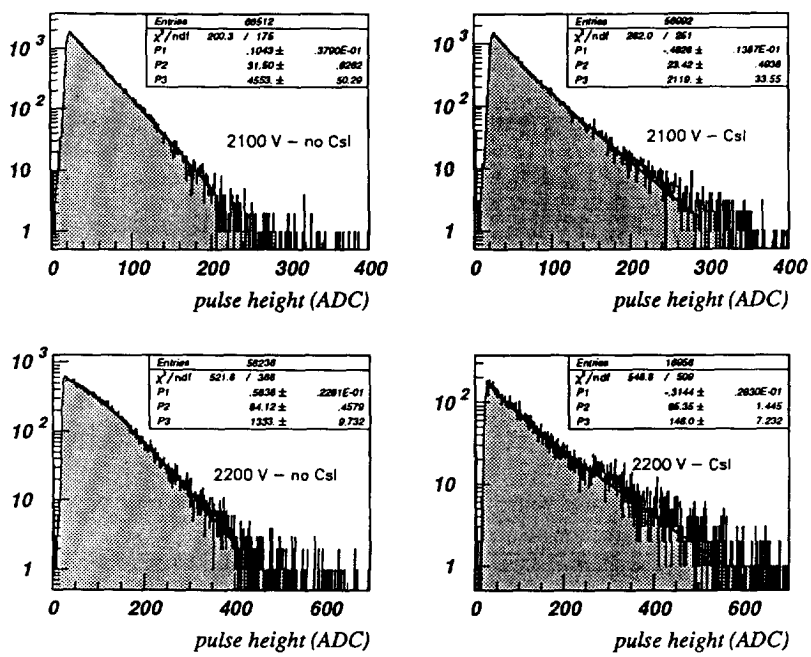

Fig. 12. PH distributions of single electrons extracted from a cathode spot surrounded (right column) or not (left column) by a CsI coating measured at two chamber gains. The constants θ and PH_0 of the Polya fit are the values of P1 and P2, respectively.

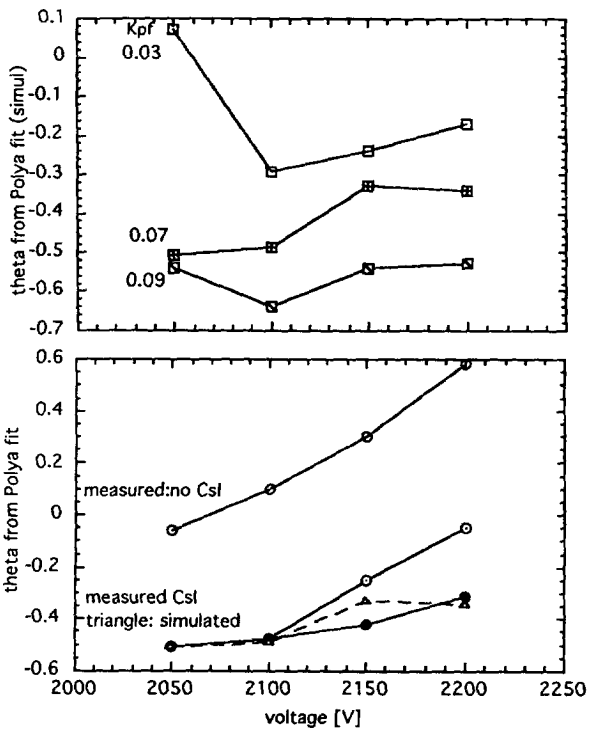

Fig. 13. θ constant from Polya fit of measured and simulated single electron PH distributions. Top: influence of the feedback photon yield constant, K_{pf}. Bottom: comparison between θ measured with or without CsI.

Polya SEPHD. Therefore, at such a high gain, the use of a Polya fit on the full PH range is no longer justified. Restricting the PH range to low values, the θ values can be approximated from a partial fit. From these first results, we can conclude that a K_{pf} value of 7.7×10^{-6} [elect.$^{-1}$] looks appropriate for generating feedback photons in CH_4. The use of a Polya fit should be restricted to low gain operation ($\leq 2 \times 10^5$) to characterize the single-electron response.

6. Results from CsI RICH and data analysis at RD-26

The QE evaluations obtained by the various investigators from measurements with CsI RICHs were outlined in Section 3.1.5, each of them describing their analysis procedure in the references quoted. We shall present here our latest results and re-examine their analysis procedure according to the preceding remarks and results related to the photon feedback and SEPHD evaluation.

6.1. Experimental conditions

Our results were obtained using a MWPC with a 2 mm anode-to-cathodes distance, a 4 mm pitch, a 20 μm wire diameter, and a pad size of $8 \times 8\,mm^2$. Five polished Cu/Ni/Au PCB substrates, described in Section 3.5.1, of sizes comprised between 1000 and 2500 cm^2 were covered with a 300 nm thick CsI film at a temperature of 50°C. They were submitted to the "heat treatment" after evaporation, that is, kept under vacuum at 50°C for 12 hours, and then mounted on the detector without being exposed to air at all. The operating gas was CH_4 but several mixtures were tested: CH_4/iC_4H_{10}, Ar/CH_4, A/iC_4H_{10}, He/iC_4H_{10} [41]. The remaining fraction of O_2 and H_2O is usually kept below 10 ppm. The radiator was filled with C_6F_{14}, circulated through an Oxysorb cartridge and contained by a 3 mm thick quartz (Suprasil II) window. The UV transparency was controlled in a monitoring cell. The thickness of the radiator could be adjusted from 0 to 15 mm by moving a screening plate inside the liquid volume. The distance from radiator to pad plane was such that 100 mm Cherenkov ring radii were obtained with pions at 3 GeV/c.

The pads were equipped with the AMPLEX or GASSIPLEX analog multiplexed electronics, achieving an input rms noise equivalent to 2000 electrons at a T_{integ} of 700 ns. The readout sensitivities were 0.39 and 0.26 fC/ADC bin for AMPLEX and GASSIPLEX, respectively. The mean threshold was 3.0 ADC bin, leading to a single photoelectron detection efficiency ≥90%. All pads were read out and the thresholds applied off-line using pedestal and rms noise tables recorded at every run.

The detector was exposed to a pion/proton beam of 3 GeV/c momentum at the CERN-PS/East area (T11 beam).

6.2. Main results

During the past three years, about 24 PCs have been analyzed at the test beam, representing about 150 days of exposure to radiation. The standard operating conditions were a total gain of 2×10^5, CH_4 circulated at 10–20 l/hour and a rate of 1 kHz/cm over a 10 cm^2 beam spot. The rate of microdischarges inducing an HV trip was less than one per week and the dark current was stable at a level of 10 nA. A fresh PC is routinely raised within 15 minutes at full operating voltage. It should be noted that this rather high stability might well be decreased by using CsI-PC of QE higher than those currently in use.

In the fall of 1994, our best QE performance was achieved [41] with PC19 by using a polished Ni/Au substrate and applying the heat post-treatment. After having detailed results obtained with that PC, we discuss our efforts to reproduce in 1995 that performance with four new PCs, referred to as PC21, PC22 of size $80 \times 20\,cm^2$, PC23 of size $50 \times 50\,cm^2$ and PC24 of size $30 \times 30\,cm^2$.

The characteristic distributions shown in Fig. 14 were measured using PC19 at 2070 V and a 10 mm radiator thickness. As described in Section 4.1, resolved clusters were selected, providing the SEPHD with a mean PH_0 =

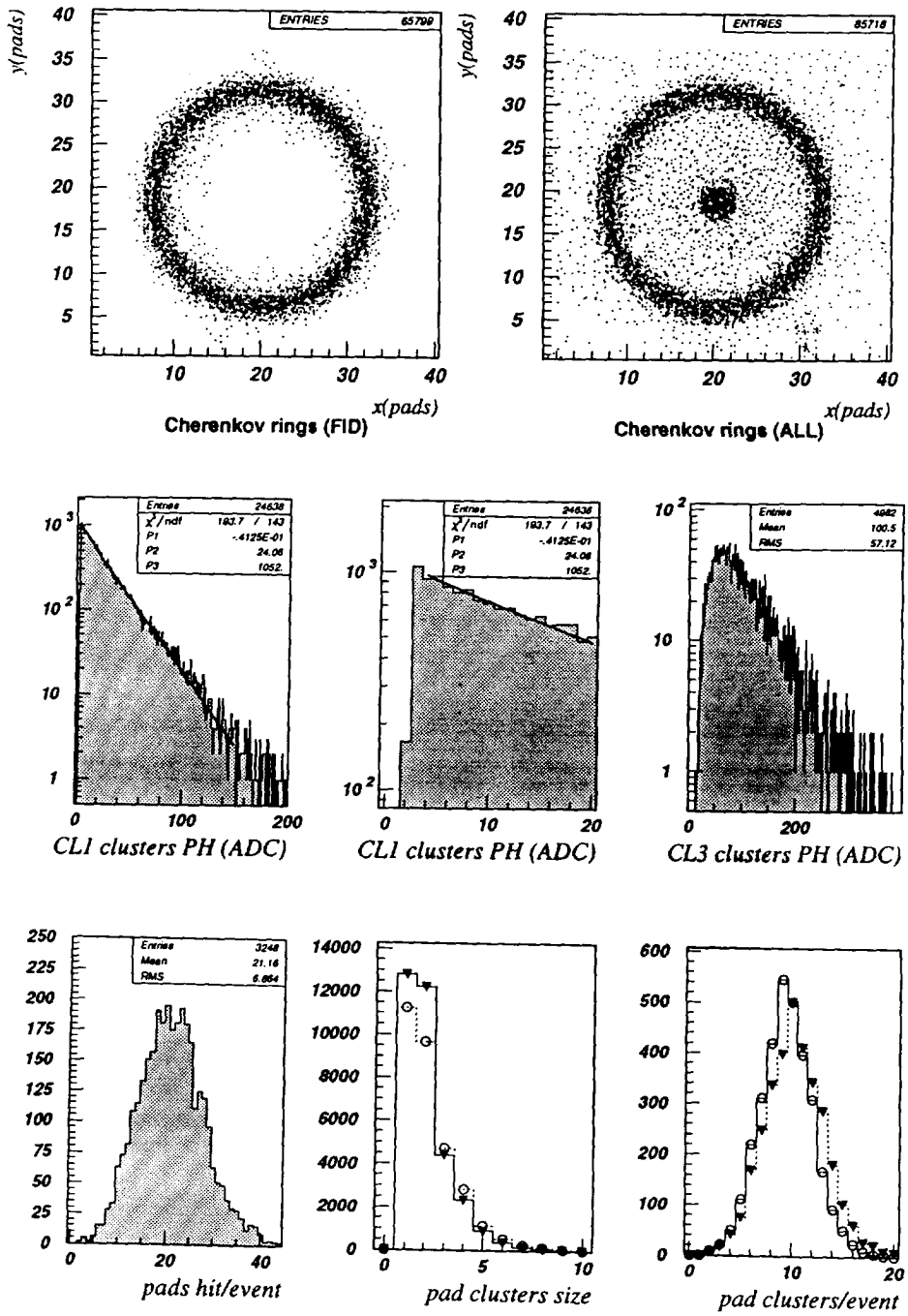

Fig. 14. Basic experimental distributions from a RD-26 Cherenkov run with PC19: 3.0 GeV/c pion, 10 mm C_6F_{14}, CH_4, 2050 V. Upper row: 3000 overlapped events into the Cherenkov fiducial zone and over the whole pad area. The smearing is due to the beam trigger area, corresponding to 1×1 cm^2. Middle row: single electron PH distribution from cluster selection, $PH_0 = 23.8$ ADC bin; zoom showing the threshold at 3.2 ADC bin, hence a 87% efficiency; Landau-like PH distribution of non-resolved clusters with several electrons per cluster. Bottom row: distribution of the number of pad hits per event, mean size and mean number per event of resolved (triangle) and raw (circle) clusters.

23.8 ADC bin and $\theta = -0.04$. The mean number of resolved clusters is 10.3 while the number of electrons obtained by dividing the total pad PH in the fiducial zone by PH_0 is 15.6. According to Fig. 9, 1.2 photons per cluster are expected from geometrical overlap probability at a radius of 100 mm, leaving an excess of 3.2 electrons to be attributed to the photon feedback contribution.

Fig. 15 shows the results obtained from the two best PCs, PC19 and PC24, when the radiator thickness was varied from 0 to 10 mm. The non-linearity of these curves indicates that the number of photons emitted per unit length increases for decreasing radiator thickness. This is due to the increase in the fraction of photons transmitted at small thickness in the lowest wavelength range where the CsI QE is the largest. At the same chamber gain, PH_0 is also found to decrease with the radiator thickness since the cluster overlap probability becomes negligible (Fig. 11). PH_0 measured at small thickness will later be used in the simulation. Note that an improvement of about 25% in these values is expected by replacing the present 74%-transparency mesh cathode by a wired one of 94%-transparency.

Fig. 16a shows the distributions of Cherenkov radii and angles. The use of C_6F_{14} allows one to obtain an angle resolution of 8 mrad per photon at a radius of 100 mm. The distribution of background events, seen outside the fiducial zone, can also be recorded in the absence of liquid in the radiator (Fig. 16b). In this case, the sources are only related to secondary photonic emission of the ionizing track, since charged deltas are drained towards the collection grid. These secondary photons may originate from the avalanche, possible gas scintillation or Cherenkov light emitted by deltas created in the quartz window.

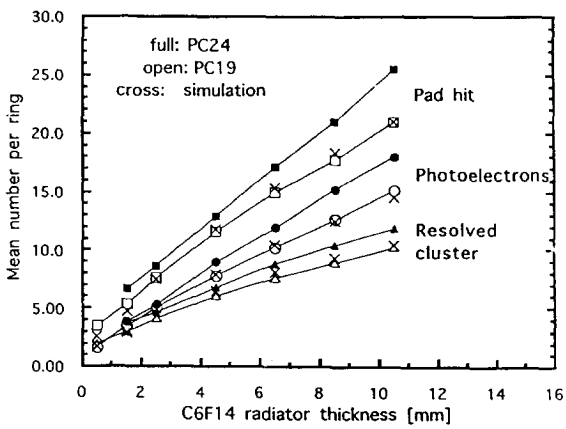

Fig. 15. Measurements of the mean numbers of pads hit, electrons and resolved clusters per ring as a function of the C_6F_{14} radiator thickness with PC19 and PC24 (CH_4, 3 GeV/c pions). The number of electrons is obtained from the total PH in the fiducial zone, and hence includes the feedback photons. The feedback photon yield used in the simulation (crosses) is $K'_{fp} = 0.07$ and the QE is shown in Fig. 18.

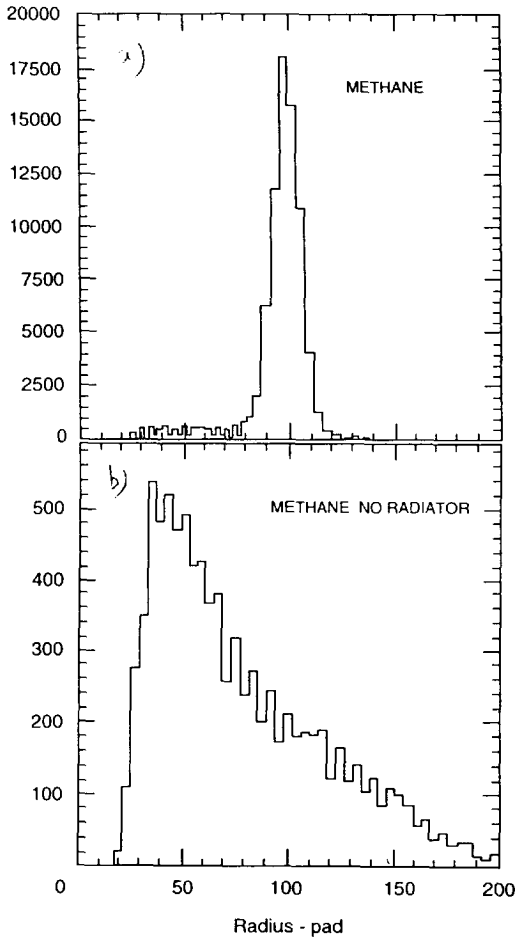

Fig. 16. (a) Distribution of the distances from the centre of the rings to each pad hit in the whole detector area showing the relative abundance of the Cherenkov peak and the background. In methane, 65% of the events have no background hit out of the Cherenkov fiducial zone. (b) The same measurement without radiator, showing the distribution of the only background events.

6.3. Simulation and discussion

The influence on the fitting procedure of the uncertainties currently affecting the quantities QE, K'_{pf}, and PH_0 is evaluated in Fig. 17a, showing simulated results obtained by varying these quantities. To fit a measurement (10 mm radiator thickness) of the mean numbers of pads and of electrons per event, two K'_{pf} values, 0.06 and 0.10, corresponding to $PH_0 = 22.0$ and 20.0, respectively, could satisfy the data, making the photon feedback contribution uncertain by about a factor 2. It can also be seen that varying the QE_{test} scaling factor affects the number of pads per event more than the number of photoelectrons, since the pads added by photon feedback generally overlap

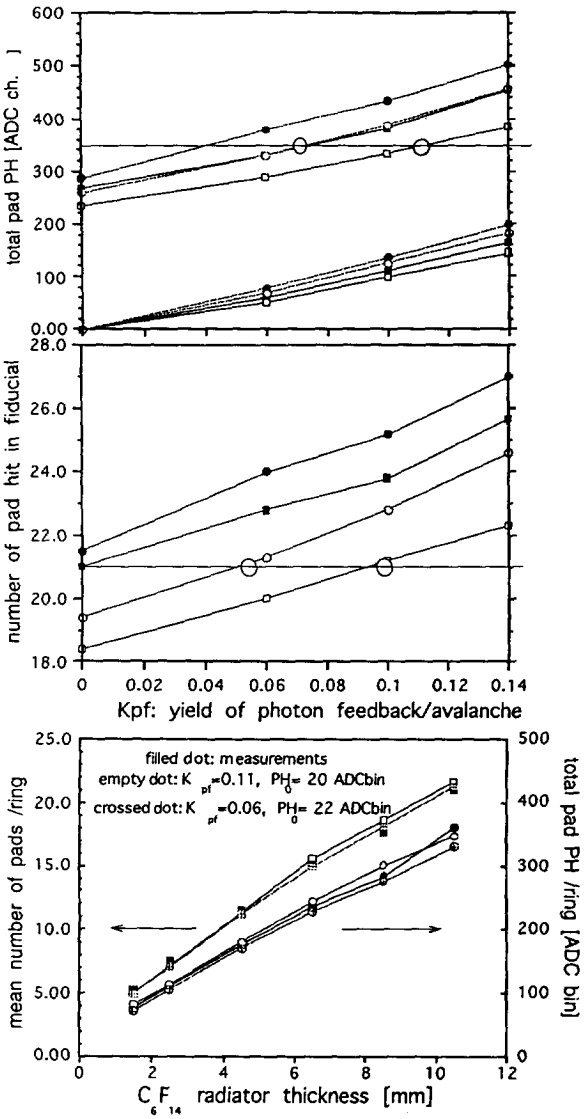

Fig. 17. (a) Influence of the feedback photon yield on the simulation. Filled/empty dots refer to QE scaling factor = 0.9/0.8. Square/circle refer to $PH_0 = 20/22$ ADC bin, respectively. The horizontal lines are the measurements and should be simultaneously fitted for the same K'_{pf} value. (b) The same exercise on the full range of measurements.

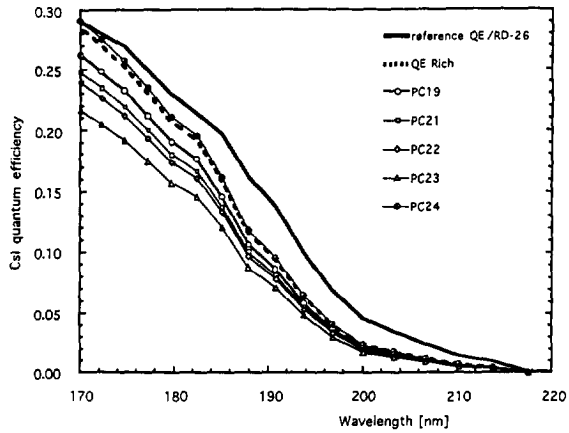

Fig. 18. QE curves used to fit the data of five larger PCs at RD-26 compared to the reference QE of Fig. 4.

with those of the primary cluster. As seen in Fig. 17b, fitting the whole set of measurements of Fig. 15 can be achieved by using two different couples (PH_0/K'_{pf}) but the same QE_{test}. To find the best QE_{test} in this case, the RD-26 QE reference must not only be scaled by a constant factor, but its shape has to be modified to reproduce the dependence of the measured number of photons emitted per unit length on the radiator thickness. This curve, QE_{Rich} in Fig. 18, shows a drop relative to the reference QE close to the photoionization threshold. Next, the fit of data obtained from different PCs can be done by simply scaling QE_{Rich} by a constant factor, as shown in Fig. 18, indicating that 72–102% of the reference was achieved on that kind of substrate. The integrals of these QE curves from the photoionization threshold to 7.3 eV (170 nm) are 0.22 for the reference and 0.13 to 0.19 for the measurements.

However, an incorrect evaluation of the feedback photon fraction has no influence on the determination of the Cherenkov radius and angle, as long as their corresponding pads are located in the Cherenkov fiducial zone. This is illustrated by the fact that no differences are found whether these quantities are calculated using the centers of every pad hit or locations calculated from cluster centroids, as seen in Fig. 19. In fact, the feedback photoelectron has the beneficial effect of reinforcing the primary signal, a property peculiar to the CsI layer and not true in gaseous photoconverters where feedback photons are converted into electrons in the whole solid angle of emission.

To simulate the background distribution of Fig. 16b, the MIP avalanches were taken as the only secondary photon sources. The ionization deposition was obtained from a Landau distribution (4 mm of CH_4) and the total charge calculated with the SEPH generator. Due to the short distance between the avalanche and the CsI surface, many photons strike the surface at a grazing incidence. Since the CsI film does not have a specular surface [30], an evaluation of the loss due to reflection, and hence of the shape of the background distribution, is made difficult. At the present time, as seen in Fig. 16b, the shape and the fraction of events without background (65%) can only be roughly simulated using a K'_{pf} value of 0.13. Other background sources, probably Cherenkov light emitted by deltas created in the quartz window, are responsible for this high K'_{pf} value. Such measurements will be pursued

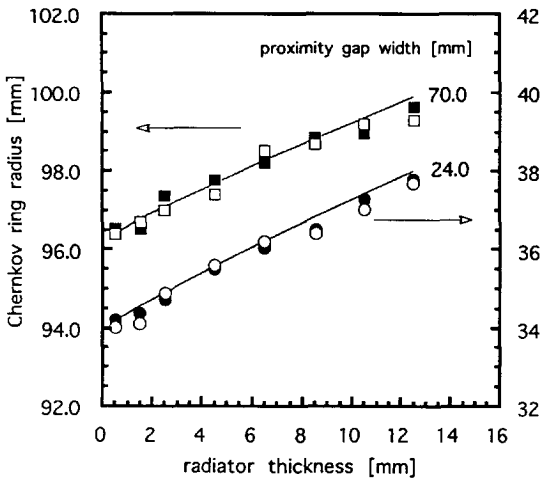

Fig. 19. Cherenkov ring radius measured as a function of the radiator thickness for two values of the proximity gap. The radii are calculated by using the centre of each pad hit (full dots) or by using cluster barycentres (empty dots). The lines show the simulated radii.

since they provide additional information on the photon feedback generation.

6.4. QE reproducibility

As seen in Fig. 18, a non-negligible spread of 30% (PC23), is still present in the QE performance of our new PCs, even though a quite satisfactory result was obtained with PC24. Noticing that the initial pressures and pressure drops were significantly different between the PC19 and PC23 processings, 6×10^{-6} to 2×10^{-6} Torr and 2×10^{-7} to 1.5×10^{-7} Torr, respectively, the following sequence of operations was performed:

– PC24 was processed, following as closely as possible the PC19 processing conditions (a controlled air peak was necessary to maintain the initial pressure at 6×10^{-6} Torr), providing a QE performance even superior to PC19,

– having measured $0.72\times QE_{RICH}$ on PC23, a 50 nm CsI film was evaporated at 6×10^{-6} Torr on top of the present film without showing any QE improvement ($0.70\times QE_{RICH}$),

– a new 300 nm CsI film was evaporated at 6×10^{-6} Torr on the PC23 substrate, showing a degradation of the QE down to $0.65\times QE_{RICH}$.

Consequently, it seems that the PC23 substrate is not behaving as well as the PC19 and PC24 ones, independently of different CsI processing conditions. Further micro-analysis studies of these substrates are in progress.

6.5. Stability and ageing

The "intrinsic" stability of the QE performance of a large PC, that is, its variation with respect to external or internal chemical agents like moisture, oxygen or reactive compounds of the substrate, was investigated by many users. The available test results tend to show a small decrease, if any, of the QE of the order of 0–10% during the first days following the evaporation. A stable level is then maintained when the PC is kept under inert gas flow. It is not possible to clearly point out any specific cause of such behaviour, given the large variety of treatments in use in these tests. A systematic control was done by Besson et al. [55] keeping two PCs under flow and low level irradiation for about one year without recording any degradation.

Under particle exposure, the main source of ageing is the impacts of the ion clouds generated by the avalanches on the CsI film. At the present time, the available results show a large spread: the same 20% QE drop is observed following exposure to an integrated charge ranging between 1.5 [22] and 20×10^{-4} C/cm^2 [33,37]. The necessary irradiation of large PCs under controlled exposure is under way in several groups at HERA, CERN, HADES, etc.

At RD-26, a 30×30 cm^2 PC (PC19) was exposed to the test beam for four periods of 3 weeks spread over a full year; the PC was kept under gas flow (Ar) between beam periods. The QE drop was evaluated at less than 8% over that year.

7. Pattern recognition and particle identification

We shall illustrate the pattern recognition performance of the CsI RICH with the results obtained from the Monte Carlo study of the ALICE PID (Section 2) where π/K separation should be achieved at densities up to 60 particles/m^2.

An "imaginary" RICH detector of 50×50 cm^2 area has been created [56] in which the raw events obtained at 3.0 GeV/c from the actual 30×30 cm^2 RICH prototype (PC19) are randomly overlapped until a required uniform density is reached. The CsI QE used is the measured value, shown in Fig. 18. It is important to note that no selection is made of the single events apart from artificially adjusting the proton/pion ratio, implying that the detector background is included. To evaluate the performance of the method used to analyse high-density data, single-ring runs are first analysed and results shown in Fig. 20, top part. The π/K 3σ separation obtained would correspond to 3.3 GeV/c particles. The results of the same procedure applied to the superimposed events are given in Fig. 20, bottom part. The results shown include only those particles that fell more than 10 cm away from the detector edges. These results are very reliable since we did not apply any cuts to the raw data. From the data in Fig. 20 it follows that the detector and analysis efficiency is close to 100% in the fiducial area at the centre of the detector also with a

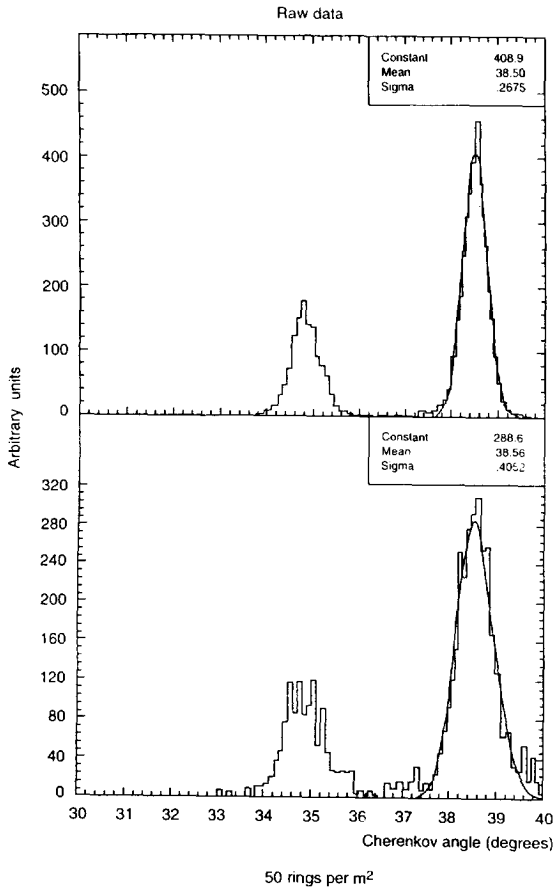

Fig. 20. Top: measured separation between pion and proton at 3 GeV/c for single particles. Bottom: the same separation using a pattern recognition algorithm applied to events with a density of 50 particles per m^2 simulated by overlapping the data taken at the test beam.

density of 60 particles per m^2. The rms is 7.0 mrad, which corresponds to a $\pi/K\ 3\sigma$ separation at 2.6 GeV/c.

The dependence of the particle separation on the incidence angle is found in Ref. [57] for a single particle at $\beta = 1$. Between 0 and 12°, the loss in photons per ring is small, 8%, increasing to 80% at 40° due to the internal reflection within the quartz window. In this Monte Carlo, the reference QE (curve 2 in Fig. 4) was used, thus providing an optimum evaluation of the separation achievable with a CsI PC. $\pi/K\ 3\sigma$ separations up to 5.2, 4.0, and 3.4 GeV/c are obtained for incidence angles of 0, 20, and 60°, respectively.

8. Conclusion

Depending on the investigator's level of optimism or on the application he has in mind, the present state of the development of large area of CsI PC to be used as photoconverters in RICH detectors can be compared to the state of a glass of wine: half-filled or half-empty. In conclusion, we shall alternatively point out positive and negative features, resulting from a large amount of contributions from many groups.

It has been demonstrated that a large area of pad electrode can be covered with CsI film using standard PCB substrates and evaporation techniques, making such a process affordable and safe. When operated under gas at atmospheric pressure in a fast RICH detector, the QE at 180 nm is found to be about 70% of the value expected from laboratory measurements, that is 0.17 ± 0.02 compared to 0.24 ± 0.02. However, the larger values observed by several groups scale these values up to a potential range of 0.25–0.35. In spite of the numerous studies of substrates, processes, treatments, etc., there is not yet a physical understanding of the causes preventing the full QE being achieved in large size detectors.

Such photoconverters, up to a quarter of m^2 in size, have been operated as the cathode of MWPCs, providing $\geq 90\%$ single-electron detection efficiency under stable operating conditions, provided that the electronics is sensitive enough to allow operation at a chamber gain $\leq 2\text{–}3 \times 10^5$. At this chamber gain, an open MWPC geometry can be used, keeping the feedback photon contribution such that the Cherenkov angle resolution is not affected. However, in this case, the maximum event rate capability is restricted to an upper limit of <1 MHz. Increasing the rate performance to the 10–20 MHz range leads to operation at a gain such that full detection efficiency can no longer be achieved due to detector instability. The only remedy seems to be to develop more sensitive fast front-end electronics. These current limitations on QE and rate make some HEP applications impossible, essentially in the p–p LHC environment. However, other future applications in heavy-ion or fixed-target experiments can already fulfil most of their requirements with the current performance.

For these kinds of applications, the manufacturing of 2–3 m^2 modules appears to be practicable since proven technologies, well known for building MWPCs equipped with VLSI front-end electronics [51] and liquid radiators [58], can be used keeping standard specifications. At present, an imaging detector with 2 CsI PCs is in operation [10], a 1.4 m^2 detector is being constructed for the HADES experiment in 1998, and the ALICE collaboration has selected the CsI RICH as a basic option for a 10 m^2 wall for high-p_t PID [59].

The next crucial milestone is to demonstrate the stability and the resistance to ageing of the CsI PC over the typical period of time required by an experiment. The first results achieved over a one year period give a satisfactory indication, to be confirmed by testing a larger area under real irradiation conditions. In this field, promising studies on protective layers [60] are under way.

Acknowledgements

I would like to acknowledge all my colleagues who have made this R&D work stimulating for many years now. I am deeply indebted to Amos Breskin and Guy Paic for their friendly and invaluable scientific contributions, to Carlo Coluzza and Jaroslav Va'vra for intense and fruitful discussions. I thank my younger colleagues, P. Martinengo, R.S. Ribeiro, A. Di Mauro and R. Puntaferro for their daily and essential work throughout this time. All of us are even more grateful to T.D. Williams, who has constantly provided us with the best apparatus, in due time, for which we thank him warmly. Special thanks to A. Braem and D. Carminati for their skill in preparing the evaporation, to E. Chesi and J.C. Santiard who took charge of the electronics, and to K. Batzner and L. Durieu for helping us at the test beam. Many thanks also to C.W. Fabjan for his constant support at NA44 and to many of our colleagues in RD-26.

References

[1] R. Arnold et al., Nucl. Instr. and Meth. A 273 (1988) 466.
[2] R. DeSalvo et al., Nucl. Instr. and Meth. A 315 (1992) 375.
[3] R. Baur et al., Nucl. Instr. and Meth. A 343 (1994) 87.
[4] P. Carlson et al., Nucl. Instr. and Meth. A 343 (1994) 198; T. Francke, these Proceedings (1995 Int. Workshop on Ring Imaging Cherenkov Detectors, Uppsala, Sweden) Nucl. Instr. and Meth. A 371 (1996) 169.
[5] M. Artuso, these Proceedings (1995 Int. Workshop on Ring Imaging Cherenkov Detectors, Uppsala, Sweden) Nucl. Instr. and Meth. A 371 (1966) 324.
[6] J. Seguinot et al., Nucl. Instr. and Meth. A 297 (1990) 133.
[7] R. Arnold et al., Report CRN/HE 91-06, CRN/Strasbourg.
[8] HADES, Proposal for a High Acceptance Di-Electron Spectrometer, GSI/Darmstadt (1993).
[9] A. Kastenmuller, presented at this Workshop.
[10] C.W. Fabjan et al., Nucl. Instr. and Meth. A 367 (1995) 240.
[11] HERA-B, Proposal, DESY-PRC 94/02.
[12] Letter of Intent, Semi-inclusive muon scattering from a polarized target, CERN/SPSLC 95-27.
[13] HERMES, Technical design report, The HERMES Collaboration (July 1993).
[14] Proposal for an electron positron collider for heavy flavor particle physics, PR-88-09, PSI, Villigen, Switzerland (1988).
[15] J. Seguinot et al., Nucl. Instr. and Meth. A 350 (1994) 430.
[16] M. French et al., Nucl. Instr. and Meth. A 324 (1993) 511.
[17] B. Ratcliff, Ref. [5], p. 309.
[18] LHC-B, Letter of Intent, CERN/LHCC 95-5.
[19] E. Nappi, Ref. [5], p. 275.
[20] Letter of Intent for A Large Ion Collider (ALICE), CERN/LHCC/93-16.
[21] Expression of Interest in a future collider detector in B0, CDF collaboration (1994).
[22] A. Breskin, Ref. [5], p. 116.
[23] RD-26 Status Report CERN/DRDC 94-49 (1994).
[24] Proc. 1st Workshop on Ring Imaging Cherenkov Detectors, Bari, Italy, 1993, Nucl. Instr. and Meth. A343 (1994) 1–326.
[25] P. Maier-Komor et al., Nucl. Instr. and Meth. A 362 (1995) 183.
[26] D.F. Anderson et al., Nucl. Instr. and Meth. A 323 (1992) 626.
[27] A. Buzulutskov et al., Nucl. Instr. and Meth. A 366 (1995) 410.
[28] C. Lu et al., Nucl. Instr. and Meth. A 343 (1994) 135.
[29] J. Almeida et al., Nucl. Instr. and Meth. A 367 (1995) 337.
[30] J. Almeida et al., Nucl. Instr. and Meth. A 361 (1995) 524.
[31] D.F. Anderson et al., Nucl. Instr. and Meth. A 326 (1993) 611.
[32] B. Surrow et al., Nucl. Instr. and Meth. A 355 (1995) 342; B. Surrow, Performance of a prototype RICH detector using a CsI photocathode readout, Thesis, State University of New York, Stoney Brook (1993).
[33] C. Lu et al., Ref. [5], p. 155.
C. Lu et al., Characterization of CsI photocathodes for use in a fast RICH detector, Princeton/HEP/94-10.
[34] W. Kononenko et al., presented at this Workshop.
[35] J. Seguinot et al., Ref. [5], p. 64.
[36] P. Krizan et a., Nucl. Instr. and Meth. A 364 (1995) 243.
[37] S. Korpar et al., Ref. [5], p. 151.
[38] R. Gernhauser et al., presented at this Workshop.
[39] R. Aleksan et al., Nucl. Instr. and Meth. A 343 (1994) 173.
[40] A. Braem et al., Nucl. Instr. and Meth. A 364 (1995) 163.
[41] J. Almeida et al., Nucl. Instr. and Meth. A 367 (1995) 332.
[42] Ph. Mine et al., Incident angle effect on the quantum efficiency of CsI photocathodes, Report X-LPNHE 94-05, Palaiseau, France.
[43] R. Arnold et al., Nucl. Instr. and Meth. A 270 (1988) 255.
[44] J. Va'vra, Ref. [5], p. 33.
[45] R. Arnold et al., Nucl. Instr. and Meth. A 314 (1992) 465.
[46] E. Gatti et al., Nucl. Instr. and Meth. 163 (1979) 83; J.S. Gordon et al., Nucl. Instr. and Meth. 227 (1984) 267 and 277.
[47] A. Di Mauro et al., Ref. [5], p. 137.
[48] A. Breskin et al., Nucl. Instr. and Meth. A, to be published.
[49] E. Beauville et al., Nucl. Instr. and Meth. A 288 (1990) 157.
[50] W. Beusch et al., Gasplex, a low noise analog signal processor for readout of gaseous detectors, Internal note 4, CERN/ECP/MIP (1993).
[51] J.C. Santiard et al., Development of a new general purpose analog signal processor with an on-chip digitizer and digital pre-processing, Internal note 2, CERN/ECP/MIP (1995).
[52] J. Byrne, Proc. Roy. Soc. Edinburgh A 66 (1962) 33.
[53] G.D. Alkhazov, Nucl. Instr. and Meth. 89 (1970) 155.
[54] J.H. Carver et al., Nucl. Instr. and Meth. 52 (1967) 130.
[55] R. Aleksan et al., Quantum efficiency and ageing tests of CsI photocatodes, Saclay DAPNIA, in preparation.
[56] A. Di Mauro et al., Nucl. Instr. and Meth. A 364 (1995) 284.
[57] A. Amadon, etude de faisabilite d'un detecteur fast-RICH pour identifier les particules a l'usine a B de SLAC, these a l'Universite de Paris XI, Orsay (1995).
[58] P. Aarnio et al., Nucl. Instr. and Meth. A 303 (1991) 233.
[59] ALICE Technical Proposal, CERN/LHCC 95-71, LHCC/P3.
[60] A. Buzulutskov et al., Ref. [5], p. 147.